mathematics

MDPI

Article

Driving Safety Analysis of Road Vehicle on Long-Span Bridge Considering Nonstationary Wind

Qinghang Li [1], Ganyu Zhou [2], Guoxing Wang [1] and Yu Feng [3,*]

[1] Shandong Pengcheng Road and Bridge Group Co., Ltd., Jining 272000, China; 15653706918@163.com (Q.L.); guoxing_wang2012@163.com (G.W.)
[2] Innovation Research Institute of Shandong High-Speed Group Co., Ltd., Jinan 250098, China; zhouganyu@stu.haut.edu.cn
[3] School of Transportation Engineering, Shandong Jianzhu University, Jinan 250101, China
* Correspondence: rainingfeng@chd.edu.cn

Abstract

Long-span bridges in mountainous areas are usually exposed to nonstationary winds (e.g., thunderstorms), which pose a significant threat to the driving safety of vehicles. However, current analysis on the wind–vehicle–bridge interaction was mainly implemented based on the assumption of stationary wind input, which would lead to the distortion in the assessment of driving safety under nonstationary extreme wind events. In this study, a nonstationary wind–vehicle–bridge coupling analysis framework was found to investigate the dynamic response and driving safety under nonstationary events. Firstly, the Wavelet–Hilbert scheme was introduced to simulate the nonstationary wind velocity, and the two-dimension indicial function was employed to model the transient aerodynamic loads. Then, the nonstationary wind–vehicle–bridge coupling system was developed, and the separate iteration method was employed to obtain the response of the coupling system. Finally, the driving safety is evaluated based on statistical accident risk coefficients, derived from wheel contact forces. The results show that the vertical contact forces transference ratio, lateral contact forces, and vehicle accident risk coefficients under nonstationary winds are higher than those resulting from equivalent stationary winds. In addition, the accident risk coefficients increase with the transient wind velocity, duration, and vehicle velocity. In particular, the risk coefficient increases by approximately 201%, 36%, and 79%, respectively, with the increase in transient wind velocity, duration, and vehicle velocity.

Keywords: nonstationary wind; wind-vehicle-bridge system; driving safety; time-domain analysis

MSC: 74F10; 74H45; 74S05

Check for updates

Academic Editors: Yiu Yin Raymond Lee and Zdeněk Kala

Received: 15 May 2026
Revised: 21 June 2026
Accepted: 23 June 2026
Published: 28 June 2026

Copyright: © 2026 by the authors. Licensee MDPI, Basel, Switzerland. This article is an open access article distributed under the terms and conditions of the Creative Commons Attribution (CC BY) license.

1. Introduction

With the rapid development of highway networks, an increasing number of long-span bridges have been constructed in complex mountainous terrains [1]. However, nonstationary wind (e.g., thunderstorms) has been frequently observed in mountainous regions [2], which would exert a significant influence on the safety of road vehicles traveling the bridge. Unfortunately, such nonsynoptic wind events would be exacerbated in the future due to global warming [3]. Therefore, a comprehensive analysis of the driving safety of the vehicle traveling on long-span bridge under nonstationary wind is essential.

The assessment of driving safety can be traced back to 1987, when Baker [4] proposed three accidents based on vehicle dynamic responses: rollover, sideslip, and yawing accidents. These criteria have been widely used for the assessment of driving safety [5,6]. Later, the driving safety indices, such as the roll safety factor [7] and the load transfer ratio [8], were subsequently developed based on Baker's foundational work. With the development of computational techniques, the interactions among wind flow, vehicle vibration, and bridge vibration were advocated to be considered in the analysis of driving safety [5,9]. The wind–vehicle–bridge interaction analysis framework was initially established by Cai and Chen [9], and has been continuously improved and increasingly applied to the analysis of driving safety [10–12]. Recently, Zhang et al. [13] introduced the aerodynamic interference effects into the wind–vehicle–bridge interaction system, and selected the load transfer ratio as a criterion to evaluate the driving safety. Chen et al. [14] utilized the load transfer ratio and sideslip factor as criteria to examine the driving safety, where the transient aerodynamic effects induced by overtaking events were considered in the coupling system. Camara [15] presents the first wind–vehicle–bridge interaction analysis framework to account for skew wind effects on driving safety. Shen et al. [16] developed a simulation model to analyze the aerodynamic characteristics of moving vehicles subjected to wake flows generated by parallel bridges. Zou et al. [17] investigated the influence of barriers on the driving safety in a wind–vehicle–bridge coupled system, where the driving behavior was considered in the driving safety evaluation framework. Fu et al. [18] introduced the concept of driver vision into the driving safety criteria, and studied the driving safety of the vehicles on the bridge under vortex-induced vibration conditions. However, the incoming winds are usually treated as a stationary random process in current research, while most overturning accidents are actually caused by nonsynoptic winds characterized by significant nonstationarity [19].

Compared to stationary boundary layer winds, nonstationary extreme winds exhibit significant time-dependent features in terms of mean, variance, and frequency composition [20–22]. In extreme wind events, wind velocity can reach multiples of the mean value within a relatively short duration [23]. Although some contributions have been made in the nonstationary winds, the focus has been primarily on wind field simulation [24] and wind-induced bridge response [25]. The investigation of the vehicle–bridge coupling system under nonstationary winds would also be required. Recently, He et al. [26] established a framework for train-bridge coupled vibration analysis under nonstationary wind conditions, highlighting the significant impact of nonstationary wind with short transient periods on train vibration. Hence, the similar influence of nonstationary wind would be expected to occur in road vehicle vibration. Hu et al. [27] investigated the driving safety of the vehicle on continuous rigid-frame bridges under nonstationary wind environments, emphasizing the noticeable nonstationary effects from fluctuating winds, especially at high wind speeds. However, only nonstationary fluctuating winds were considered in this study, and the influence of time-varying mean wind was neglected. Therefore, it is necessary to develop a complete framework for nonstationary wind–vehicle–bridge interaction coupled analysis, and investigate the driving safety and performance of the coupling system in nonstationary wind events.

In this study, the wind–vehicle–bridge coupling system under nonstationary wind was first established in Section 2, where the modeling of nonstationary wind fields and the aerodynamic loads were introduced. Then, the vehicle accident assessment criteria and their statistical values were formulated in Section 3. Finally, the analysis of wind–vehicle–bridge coupled vibration and assessment of driving safety under nonstationary wind was performed in Section 4.

2. Vehicle–Bridge Interaction System Under Nonstationary Wind

2.1. Modeling of Vehicle and Bridge

2.1.1. Vehicle Model

The analytical model for each vehicle can be established using a multibody dynamics method, in which the vehicle body and wheels are modeled as rigid bodies connected through spring–damper suspension systems [9]. The 2-axle vehicle with 13 degrees of freedom is selected to investigate dynamic response and evaluate driving safety as shown in Figure 1. The equation of motion for the vehicle can be derived based on D'Alembert method, summarized as follows:

$$\boldsymbol{M}_v\ddot{\boldsymbol{x}}_v + \boldsymbol{C}_v\dot{\boldsymbol{x}}_v + \boldsymbol{K}_v\boldsymbol{x}_v = \boldsymbol{F}_v \tag{1}$$

where $\boldsymbol{M}_v$, $\boldsymbol{C}_v$, and $\boldsymbol{K}_v$ are the mass, damping, and stiffness matrices of vehicle, respectively. $\boldsymbol{F}_v$ is the external load acting on the vehicle from wind and road surface roughness. $\ddot{\boldsymbol{x}}_v$, $\dot{\boldsymbol{x}}_v$, $\boldsymbol{x}_v$ are the acceleration, velocity, and displacement vectors of vehicle, respectively, and the displacement vector can be expressed as

$$x_v = [Z_v\ Y_v\ \theta_v\ \varphi_v\ \phi_v\ Z_{w1}\ Y_{w1}\ Z_{w2}\ Y_{w2}\ Z_{w3}\ Y_{w3}\ Z_{w4}\ Y_{w4}] \tag{2}$$

where Z_v and Y_v are the vertical and lateral displacements of the body, and θ_v, φ_v, and ϕ_v are the pitching, yawing, and rolling displacements of the body. $Z_{wi}(i = 1, 2, 3, 4)$ and $Y_{wi}(i = 1, 2, 3, 4)$ are the vertical and lateral displacements of the wheels i.

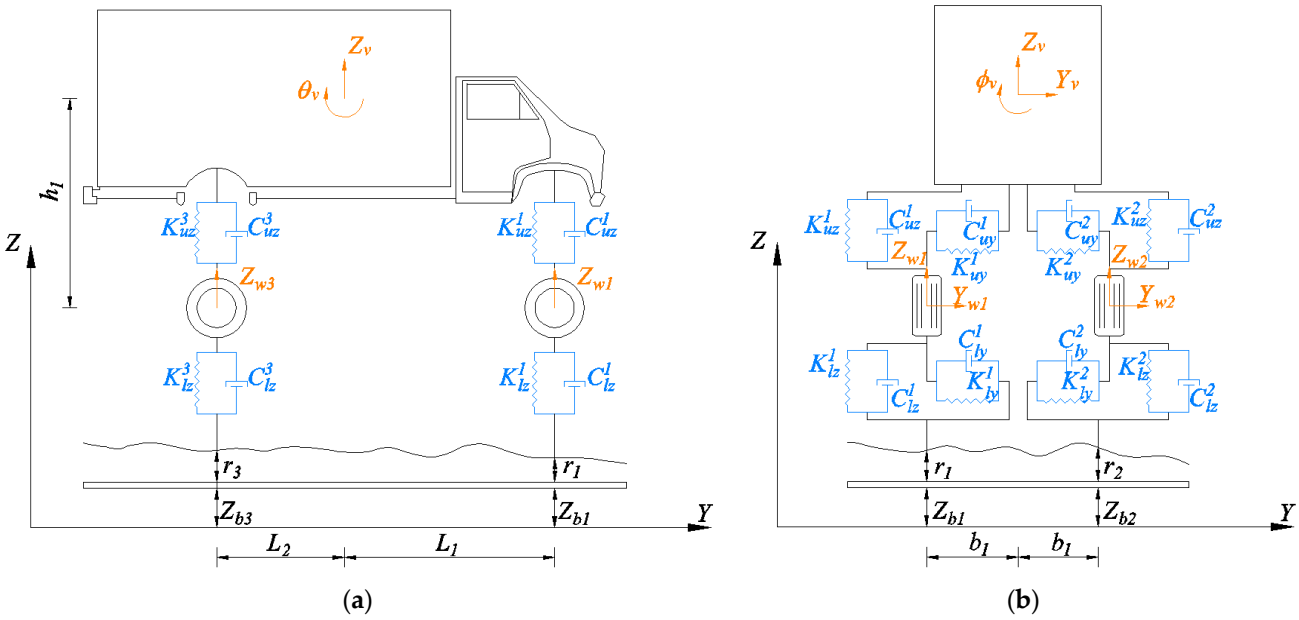


Figure 1. 13-DOFs vehicle model: (**a**) Elevation view. (**b**) Side view.

2.1.2. Bridge Model

The finite element scheme is selected to build the bridge model for simulation [28,29]. The beam elements are used to model the main girder, towers, and piers, while the link elements are used to model the stay cables. Additionally, the mass elements are applied to represent the mass characteristics of the bridge deck (e.g., deck paving). The mass and stiffness matrices of the bridge are directly obtained from the finite element model, and the

damping matrix is formulated based on the Rayleigh damping assumption. The equation of motion for the bridge can be expressed as

$$\boldsymbol{M_b}\ddot{\boldsymbol{x}}_{\boldsymbol{b}} + \boldsymbol{C_b}\dot{\boldsymbol{x}}_{\boldsymbol{b}} + \boldsymbol{K_b}\boldsymbol{x_b} = \boldsymbol{F_b} \tag{3}$$

where $\boldsymbol{M_b}$, $\boldsymbol{C_b}$, and $\boldsymbol{K_b}$ are the mass, damping, and stiffness matrices of bridge, and $\boldsymbol{F}_b$ is the external load on the bridge due to wind, vehicle, and road surface roughness. $\ddot{\boldsymbol{x}}_{\boldsymbol{b}}$, $\dot{\boldsymbol{x}}_{\boldsymbol{b}}$, $\boldsymbol{x_b}$ are the acceleration, velocity, and displacement vectors of bridge, respectively.

2.1.3. Vehicle–Bridge Interaction Relationship

The vibration of the vehicle on deck would excite a response on the bridge, while the bridge vibrations, in turn, feed back into the vehicle. This interaction between vehicle and bridge would change the dynamic characteristics of both systems. The interaction relationship is primarily reflected in the two aspects: displacement and force equilibrium [13]. The wheel loads are assumed to be point loads and never separated from deck. The contact force at each wheel in the vehicle–bridge system can be expressed as

$$F^i_{bv,z} = -F^i_{vb,z} = K^i_{lz}\Delta Z^i_l + C^i_{lz}\dot{\Delta Z}^i_l \tag{4}$$

$$F^i_{bv,y} = -F^i_{vb,y} = K^i_{ly}\Delta Y^i_l + C^i_{ly}\dot{\Delta Y}^i_l \tag{5}$$

where $F^i_{bv,z}$ and $F^i_{vb,z}$ are the vertical contact forces between wheel and deck; $F^i_{bv,y}$ and $F^i_{vb,y}$ are the lateral forces contact forces between wheel and deck; ΔZ^i_l and ΔY^i_l are the vertical and lateral displacements of the lower suspension system. The displacements of the lower suspension system can be expressed as

$$\Delta Z^i_l = Z_{wi} - Z_{bi} + r_i \tag{6}$$

$$\Delta Y^i_l = Y_{wi} - Y_{bi} \tag{7}$$

where $r_i (i = 1, 2, 3, 4)$ is the road surface roughness at the wheel i; Z_{bi} and Y_{bi} are the vertical and lateral bridge deck displacements at the wheel contact point, respectively. The displacement contact relationship in fish-bone bridge model is illustrated in Figure 2, and bridge deck displacements at the wheel contact point can be expressed as

$$Z_{bi} = u_z + \theta_x e_{yi} \tag{8}$$

$$Y_{bi} = u_y + \theta_x e_{zi} \tag{9}$$

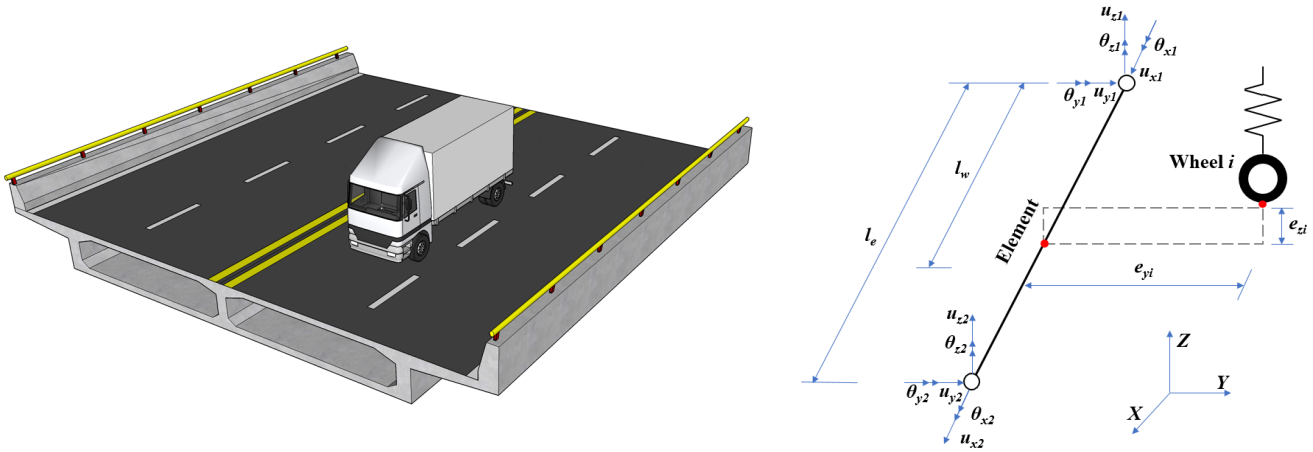
where u_z and u_y are the vertical and lateral displacements at the centroid of beam, respectively, and θ_x is the torsional displacement at the centroid of beam. e_{yi} and e_{zi} are the vertical and horizontal distances from the wheel contact point to the centroid of beam, respectively. When the wheel does not locate at the node, the displacements can be interpolated based on shape functions:

$$u_z = N_1 u_{z1} + N_2 \theta_{y1} + N_3 u_{z2} + N_4 \theta_{y2} \tag{10}$$

$$u_y = N_1 u_{y1} + N_2 \theta_{y1} + N_3 u_{y2} + N_4 \theta_{y2} \tag{11}$$

$$\theta_x = N_5 \theta_{x1} + N_6 \theta_{x2} \tag{12}$$

where $N_1 = 1 - 3l^2_w/l^2_e + 2l^3_w/l^3_e$, $N_2 = l_w - 2l^2_w/l_e + 2l^3_w/l^2_e$, $N_3 = 3l^2_w/l^2_e - 2l^3_w/l^3_e$, $N_4 = -l^2_w/l_e + l^3_w/l^2_e$, $N_5 = l_w/l_e$, $N_5 = 1 - l_w/l_e$. Similarly, the contact forces at the wheel locations can also be transferred to the nodes of the finite element model through an inverse operation of the shape functions.



(**a**) (**b**)

Figure 2. Displacement contact relationship between wheel and deck: (**a**) Diagram of a vehicle on deck. (**b**) Displacement contact relationship (The red points present the contact point of wheels and corresponding positions of beam elements).

2.2. Nonstationary Wind Loads

The wind loads acting on the vehicle–bridge system can be mainly divided into three main components during extreme wind events: static wind force, buffeting force, and self-excited force induced by time-varying mean wind, gust wind, and deck motion, respectively.

2.2.1. Simulation of Nonstationary Wind

The half-sine wave model, proposed by Kwon and Kareem [30], was selected to model the time-varying mean wind in nonstationary wind events, which is usually applied to the analysis of wind-induced responses in nonstationary wind events [26]:

$$U(t) = \begin{cases} U_0 & others \\ U_0 + U_{acc}\sin[(t-t_0)\pi/T] & t_0 < t < t+T \end{cases} \tag{13}$$

where U_0 is the initial wind velocity; t_0 is the initial time of the transient wind; U_{acc} and T are the transient wind velocity and duration, respectively. The time-varying mean wind described in Equation (13) is schematically shown in Figure 3. U_e represents the equivalent constant mean wind velocity obtained by the mean of wind velocity duration D_t (D_t represents the time during which the vehicle travels on the bridge).

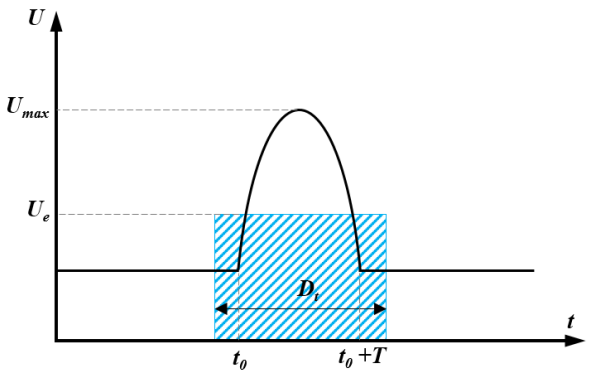


Figure 3. Schematic diagram of time-varying mean wind.

Considering the time-dependent spectrum of nonstationary fluctuating wind, the Wavelet–Hilbert-based scheme was widely utilized in the simulation of nonstationary processes [31,32]. The Hilbert transform (HT) could exactly extract the transient features

of nonstationary signals, and the wavelet transform (WT) can better preserve the spectral information and probability distribution characteristics of the instantaneous frequency [33]. The detailed process is plotted in Figure 4.

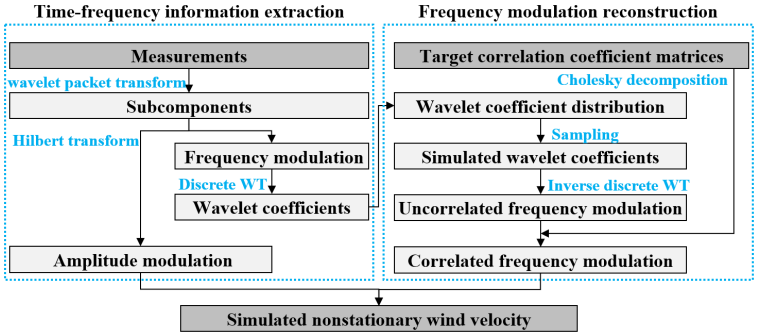


Figure 4. Procedure of nonstationary fluctuating wind simulation.

2.2.2. Nonstationary Wind Loads on Bridge

Under the quasi-steady assumption, the time-varying static wind loads on bridge deck can be expressed as [34]:

$$D_{b,st} = \frac{1}{2}\rho U(t)^2 C_D B \tag{14}$$

$$L_{b,st} = \frac{1}{2}\rho U(t)^2 C_L B \tag{15}$$

$$M_{b,st} = \frac{1}{2}\rho U(t)^2 C_M B^2 \tag{16}$$

where ρ is the air density; B is the deck width; C_D, C_L, and C_M are the static aerodynamic force coefficients.

Additionally, the motion-induced self-excited forces can be described using indicial functions in the time domain, because of their more physically sound interpretation of wind effects on a bluff body [35]. Considering the transient effects of nonstationary wind on bridges, a two-dimensional indicial function is adopted for modeling aerodynamic forces. Hence, the self-excited force can be expressed as [36]:

$$\begin{aligned} D_{b,se} = \tfrac{1}{2}\rho U(t)^2 B C'_D \quad & \left\{ \left[\varphi_{Dp}[t, U(0)]\dot{p}(0)/U(0) + \int_0^t \varphi_{Dp}[t-\tau, U(\tau)]\ddot{p}(\tau)/U(\tau)d\tau \right] \right. \\ & + \left[\varphi_{Dh}[t, U(0)]\dot{h}(0)/U(0) + \int_0^t \varphi_{Dh}[t-\tau, U(\tau)]\ddot{h}(\tau)/U(\tau)d\tau \right] \\ & \left. + \left[\varphi_{D\alpha}[t, U(0)]\alpha(0) + \int_0^t \varphi_{D\alpha}[t-\tau, U(\tau)]\dot{\alpha}(\tau)d\tau \right] \right\} \end{aligned} \tag{17}$$

$$\begin{aligned} L_{b,se} = \tfrac{1}{2}\rho U(t)^2 B C'_L \quad & \left\{ \left[\varphi_{Lp}[t, U(0)]\dot{p}(0)/U(0) + \int_0^t \varphi_{Lp}[t-\tau, U(\tau)]\ddot{p}(\tau)/U(\tau)d\tau \right] \right. \\ & + \left[\varphi_{Lh}[t, U(0)]\dot{h}(0)/U(0) + \int_0^t \varphi_{Lh}[t-\tau, U(\tau)]\ddot{h}(\tau)/U(\tau)d\tau \right] \\ & \left. + \left[\varphi_{L\alpha}[t, U(0)]\alpha(0) + \int_0^t \varphi_{L\alpha}[t-\tau, U(\tau)]\dot{\alpha}(\tau)d\tau \right] \right\} \end{aligned} \tag{18}$$

$$\begin{aligned} M_{b,se} = \tfrac{1}{2}\rho U(t)^2 B^2 C'_M \quad & \left\{ \left[\varphi_{Mp}[t, U(0)]\dot{p}(0)/U(0) + \int_0^t \varphi_{Mp}[t-\tau, U(\tau)]\ddot{p}(\tau)/U(\tau)d\tau \right] \right. \\ & + \left[\varphi_{Mh}[t, U(0)]\dot{h}(0)/U(0) + \int_0^t \varphi_{Mh}[t-\tau, U(\tau)]\ddot{h}(\tau)/U(\tau)d\tau \right] \\ & \left. + \left[\varphi_{M\alpha}[t, U(0)]\alpha(0) + \int_0^t \varphi_{M\alpha}[t-\tau, U(\tau)]\dot{\alpha}(\tau)d\tau \right] \right\} \end{aligned} \tag{19}$$

where $C'_D = \mathrm{d}C_D/\mathrm{d}\alpha$; $C'_L = \mathrm{d}C_L/\mathrm{d}\alpha$; $C'_M = \mathrm{d}C_M/\mathrm{d}\alpha$; p, h, and α are the horizontal, vertical, and torsional motion, respectively, and overdot represents the derivative with respect to the physical time; $\varphi_{yx}[t, U(\tau)]$ $(y = D, L, M; x = p, h, \alpha)$ is 2D indicial function, which could be fitted based on the flutter derivative measured in wind tunnel test [36].

Similarly, the buffeting force load can also be expressed based on the 2D aerodynamic indicial functions as

$$D_{b,bu} = \frac{1}{2}\rho U(t)^2 B\{2C_D\left[\psi_{D(u/U)}[t,U(0)]\frac{u(0)}{U(t)} + \int_0^t \psi_{D(u/U)}[t-\tau,U(\tau)]\frac{\dot{u}(\tau)}{U(\tau)}d\tau\right] + (C'_D - C_L)\left[\psi_{D(w/U)}[t,U(0)]\frac{w(0)}{U(t)} + \int_0^t \psi_{D(w/U)}[t-\tau,U(\tau)]\frac{\dot{w}(\tau)}{U(\tau)}d\tau\right]\} \quad (20)$$

$$L_{b,bu} = \frac{1}{2}\rho U(t)^2 B\{2C_L\left[\psi_{L(u/U)}[t,U(0)]\frac{u(0)}{U(t)} + \int_0^t \psi_{L(u/U)}[t-\tau,U(\tau)]\frac{\dot{u}(\tau)}{U(\tau)}d\tau\right] + (C_D + C'_L)\left[\psi_{L(w/U)}[t,U(0)]\frac{w(0)}{U(t)} + \int_0^t \psi_{L(w/U)}[t-\tau,U(\tau)]\frac{\dot{w}(\tau)}{U(\tau)}d\tau\right]\} \quad (21)$$

$$M_{b,bu} = \frac{1}{2}\rho U(t)^2 B^2\left\{2C_M\left[\psi_{M(u/U)}[t,U(0)]\frac{u(0)}{U(t)} + \int_0^t \psi_{M(u/U)}[t-\tau,U(\tau)]\frac{\dot{u}(\tau)}{U(\tau)}d\tau\right] + C'_M\left[\psi_{M(w/U)}[t,U(0)]\frac{w(0)}{U(t)} + \int_0^t \psi_{M(w/U)}[t-\tau,U(\tau)]\frac{\dot{w}(\tau)}{U(\tau)}d\tau\right]\right\} \quad (22)$$

where $\psi[t,U(\tau)]$ is 2D aerodynamic indicial function, and u and w are the horizontal and vertical fluctuating wind.

2.2.3. Nonstationary Wind Loads on Vehicle

The vehicle is assumed to travel the bridge at a constant speed in this study. The static wind loads acting on the vehicle can be obtained based on the quasi-steady assumption [37]:

$$F_{i,st} = \frac{1}{2}\rho U_R(t)^2 C_i A_f \ (i = D,S,L) \quad (23)$$

$$M_{i,st} = \frac{1}{2}\rho U_R(t)^2 C_i A_f h_1 \ (i = R,Y,P) \quad (24)$$

where A_f is the frontal area of vehicle; h_1 is the height from the gravity center of the vehicle to the ground; C_i is aerodynamic coefficient of vehicle, and subscript D,S,L,R,Y,P represent drag force, side force, lift force, rolling moment, yawing moment, and pitching moment. The aerodynamic coefficient of vehicle varies with the yaw angle ($\psi = \text{atan}(U_W/U_V)$). U_R is resultant wind velocity, determined by vehicle velocity (U_V) and wind velocity (U_W) [38]. Figure 5 illustrates the vector relationships of resultant wind velocity, vehicle velocity, and wind velocity.

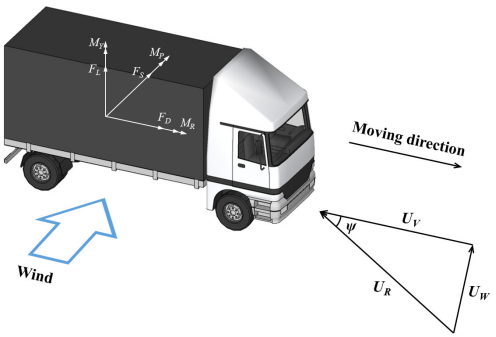


Figure 5. Vector relationship of vehicle velocity and wind velocity.

According to the linear quasi-steady buffeting model, the buffeting loads on the vehicle, which ignore the aerodynamic admittance, are expressed as [13]:

$$F_{i,bu} = \frac{1}{2}\rho U_R(t)^2 A_f\left[2C_i\frac{u(t)}{U_R(t)} + C'_i\frac{w(t)}{U_R(t)}\right](i = D,S,L) \quad (25)$$

$$M_{i,st} = \frac{1}{2}\rho U_R(t)^2 A_f h_v\left[2C_i\frac{u(t)}{U_R(t)} + C'_i\frac{w(t)}{U_R(t)}\right](i = R,Y,P) \quad (26)$$

where $C'_i(i = D, S, L, R, Y, P)$ denotes the derivatives of the aerodynamic coefficients with respect to the wind angle of attack.

2.3. Numerical Solution Method

The equations of motion for the wind–vehicle–bridge coupling system are established in the static equilibrium position, as follows:

$$\boldsymbol{M}_v\ddot{\boldsymbol{x}}_v + \boldsymbol{C}_v\dot{\boldsymbol{x}}_v + \boldsymbol{K}_v\boldsymbol{x}_v = \boldsymbol{F}_{vb} + \boldsymbol{F}_{v,st} + \boldsymbol{F}_{v,bu} \tag{27}$$

$$\boldsymbol{M}_b\ddot{\boldsymbol{x}}_b + \boldsymbol{C}_b\dot{\boldsymbol{x}}_b + \boldsymbol{K}_b\boldsymbol{x}_b = \boldsymbol{F}_{bv} + \boldsymbol{F}_{b,st} + \boldsymbol{F}_{b,bu} + \boldsymbol{F}_{b,se} \tag{28}$$

where subscripts b and v represent the bridge and vehicle subsystems; $\boldsymbol{F}_{vb}$ and $\boldsymbol{F}_{bv}$ are the vehicle–bridge interaction forces; $\boldsymbol{F}_{v,st}$ and $\boldsymbol{F}_{v,bu}$ are the static wind and buffeting load vectors on the vehicle, as given in Equations (25)~(28); $\boldsymbol{F}_{b,st}$, $\boldsymbol{F}_{b,bu}$, and $\boldsymbol{F}_{b,se}$ are the static wind, buffeting, and self-excited loads on the bridge, as expressed in Equations (14)~(22).

The equations of motion for the wind–vehicle–bridge coupling system are time-dependent due to the movement of vehicles along the bridge deck. Hence, time-consuming system matrix updating is required at each time step [39]. To improve computational efficiency, the separate iteration method [9,40] will be employed for the analysis of vehicle–bridge coupled vibration under nonstationary winds. At each time step, the positions of the wheel–bridge contact points are first determined, and the relationships between the displacements/forces at these contact points and the nodal displacements/forces of the bridge model are established by the shape functions. Subsequently, the vehicle and bridge subsystems are solved independently using the Newmark method with wind forces and vehicle–bridge interaction forces considered. Finally, an equilibrium iteration is conducted to obtain the converged response of the coupled system, and the next time step will be performed. The detailed procedure is plotted in Figure 6. The wind–vehicle–bridge coupling system analysis module was prepared adopting the above method based on Visual Fortran and embedded into the self-developed bridge dynamic analysis software BDANS (v 1.0, Bridge Dynamic Analysis System) [41].

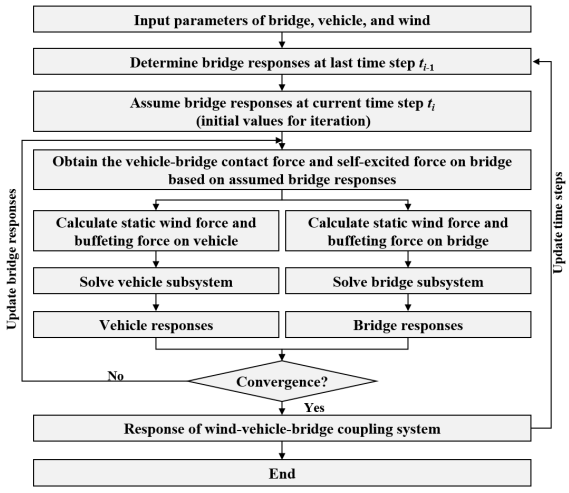


Figure 6. Procedure of coupling system solution based on separate iteration method.

3. Wind-Induced Accident Assessment Criteria for Vehicles

The driving safety plays a critical role in ensuring the efficiency of transportation routes, but nonstationary extreme winds pose significant challenges to driving safety [17]. There are three typical vehicle accidents: rollover, sideslip, and yawing accidents. The rollover accident is usually considered to occur when the vertical contact force of any

wheels becomes zero. However, a sudden drop in the road surface roughness would also unload the vertical contact forces. This phenomenon does not mean the rollover accident, because the stability of vehicle could be supported by the other wheels. Hence, the rollover accident can be evaluated based on the transference ratio of contact forces from the windward wheels to the leeward wheel. The risk coefficient for the rollover accident was expressed as [11]:

$$\eta_r = \left| \frac{\sum_{i=1}^{N} \left[F_{Lz}^i(t) - F_{Wz}^i(t) \right]}{\sum_{i=1}^{N} \left[F_{Lz}^i(t) + F_{Wz}^i(t) \right]} \right| \tag{29}$$

where $F_{Lz}^i(t)$ and $F_{Wz}^i(t)$ are vertical contact forces of the leeward and windward wheel installed on the i-th axle, respectively; N is the number of axles, and $N = 2$ was selected in this case. Clearly, a larger risk coefficient indicates a higher probability of rollover accidents.

The sideslip accident is assumed to occur when the lateral contact force exceeds the frictional force limit between wheel and bridge. The risk coefficient for the sideslip accident can be expressed as

$$\eta_s = \left| \frac{F_{Ly}^i(t) + F_{Wy}^i(t)}{\mu_s \left[F_{Lz}^i(t) + F_{Wz}^i(t) \right]} \right| \tag{30}$$

where $F_{Ly}^i(t)$ and $F_{Wy}^i(t)$ are lateral contact forces of leeward and windward wheel of the lightest axle; μ_s is the friction coefficient, which can be set to 0.7 and 0.5 for dry and wet road surfaces, respectively [42]. Similarly, a larger risk coefficient implies a higher probability of sideslip accidents. Considering yawing accidents susceptible to human factors (e.g., driving behavior), they are not addressed in this study [13].

4. Numerical Examples

4.1. Analytical Parameters

(1) Long-span bridge

The Jizou bridge, a cable-stayed bridge with a total length of 466 m, is employed to investigate vehicle–bridge coupled vibration under nonstationary winds (see in Figure 7). The finite element model of the bridge is established following the method introduced in Section 2.1.2. The geometric nonlinearity induced by cable sag effects is be modified using the Ernst equation. The modal properties that significantly influence the dynamic response of bridge are summarized in Table 1.

According to the study by Han et al. [10], the aerodynamic interference from road vehicles on the bridge is limited. Hence, the aerodynamic parameters of the bridge were measured with vehicles ignored. The aerodynamic coefficients and flutter derivatives of the bridge are presented in Figures 8 and 9, which may be obtained through wind tunnel tests or computational fluid dynamics (CFD) technique.

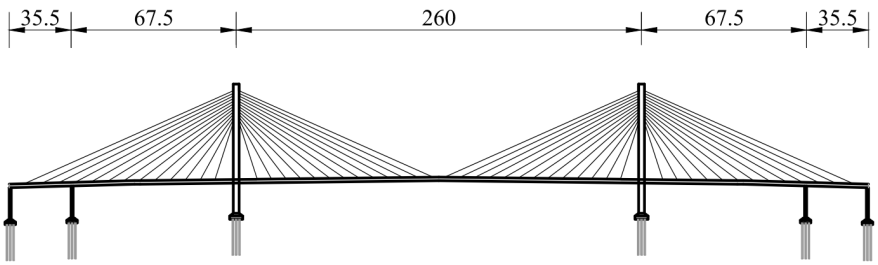


Figure 7. Elevation configuration of example bridge (unit: m).

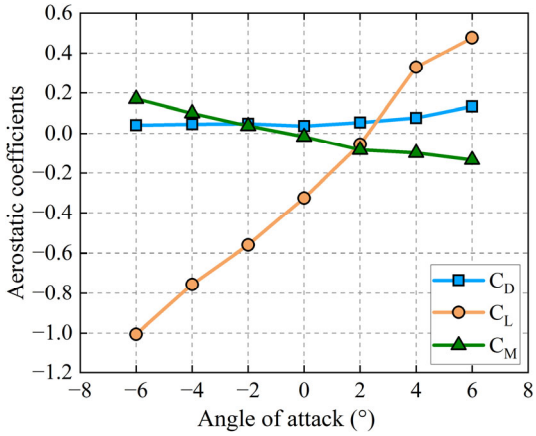


Figure 8. Aerostatic coefficients.

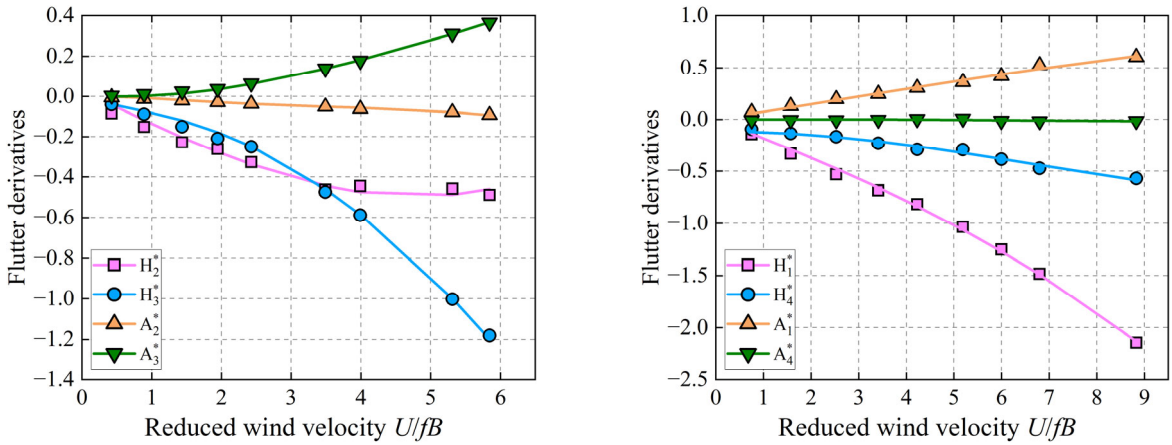


Figure 9. Flutter derivatives.

Table 1. Critical modal frequencies of example bridge.

Order	Frequency (Hz)	Mode Shape [1]
2	0.5509	L-S-1
3	0.5750	V-S-1
4	0.8410	V-A-1
5	1.2192	T-A-1
6	1.2792	V-S-2
8	1.4467	L-A-1
10	1.7383	V-A-2
11	1.8235	T-S-1
14	2.3322	T-S-2
16	2.6423	V-S-3
17	2.7320	L-S-2
18	2.9233	T-A-2

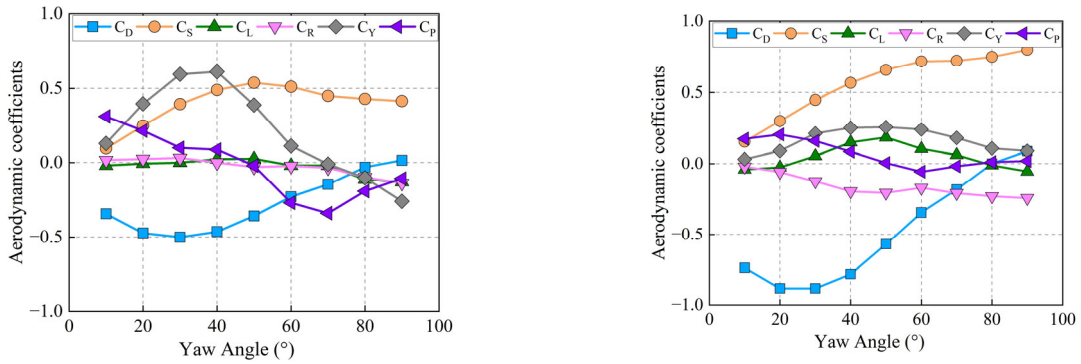
[1] V = Vertical, L = lateral, T = Torsional, S = Symmetric, and A = Asymmetric.

(2) Vehicles

Two common types of vehicles (i.e., sedan and truck) are employed to evaluate driving safety under nonstationary wind. The vehicle model was established based on the D'Alembert method described in Section 2.1.1. The dynamic and geometric parameters of the sedan and truck are listed in Table 2, and the aerodynamic coefficients of the vehicle are presented in Figure 10.

Table 2. Dynamic and geometric parameters of vehicle.

Parameters	Description	Unit	Sedan	Truck
M_v	Mass of body	kg	1600	3280
J_x	Rolling moment of inertia of body	kg·m^2	471	1349
J_y	Pitching moment of inertia of body	kg·m^2	1732	5516
J_z	Yawing moment of inertia of body	kg·m^2	3000	5000
$K_{uz}^i (i = 1,2)$	Upper vertical stiffness for 1st axle	kN/m	109	300
$K_{uz}^i (i = 3,4)$	Upper vertical stiffness for 2nd axle	kN/m	109	300
$K_{uy}^i (i = 1,2)$	Upper lateral stiffness for 1st axle	kN/m	69.5	200
$K_{uy}^i (i = 3,4)$	Upper lateral stiffness for 2nd axle	kN/m	69.5	200
$K_{lz}^i (i = 1,2)$	Lower vertical stiffness for 1st axle	kN/m	70	225
$K_{lz}^i (i = 3,4)$	Lower vertical stiffness for 2nd axle	kN/m	70	225
$K_{ly}^i (i = 1,2)$	Lower lateral stiffness for 1st axle	kN/m	58.7	121
$K_{ly}^i (i = 3,4)$	Lower lateral stiffness for 2nd axle	kN/m	58.7	121
$C_{uz}^i (i = 1,2)$	Upper vertical damping coefficient for 1st axle	kN·s/m	0.8	2.5
$C_{uz}^i (i = 3,4)$	Upper vertical damping coefficient for 2nd axle	kN·s/m	0.8	2.5
$C_{uy}^i (i = 1,2)$	Upper lateral damping coefficient for 1st axle	kN·s/m	0.8	2.5
$C_{uy}^i (i = 3,4)$	Upper lateral damping coefficient for 2nd axle	kN·s/m	0.8	2.5
$C_{lz}^i (i = 1,2)$	Lower vertical damping coefficient for 1st axle	kN·s/m	0.5	1.0
$C_{lz}^i (i = 3,4)$	Lower vertical damping coefficient for 2nd axle	kN·s/m	0.5	1.0
$C_{ly}^i (i = 1,2)$	Lower lateral damping coefficient for 1st axle	kN·s/m	0.5	1.0
$C_{ly}^i (i = 3,4)$	Lower lateral damping coefficient for 2nd axle	kN·s/m	0.5	1.0
L_1	Distance the centroid to 1st axle	m	1.15	3.04
L_2	Distance the centroid to 2nd axle	m	1.71	1.96
h_1	Reference height	m	0.43	1.5
A_f	Frontal area	m^2	4.63	20.1



(**a**) (**b**)

Figure 10. Aerodynamic coefficients of vehicle: (**a**) Sedan; (**b**) Truck.

(3) Road surface roughness

The road surface roughness is one of the main excitation sources for the wind–vehicle–bridge coupling system [14]. In this study, the road surface roughness is assumed to be a zero-mean Gaussian random process [43], and the road surface roughness at the leeward wheel can be expressed as

$$R_L(x) = \sum_i^N \sqrt{2G(n_i)\Delta n}\cos(2\pi n_i x + \theta_i) \tag{31}$$

where N is the number of discrete frequencies; Δn is the frequency increment; n_i is i-th spatial frequency point; θ_i is the random phase uniformly distributed between 0 and 2π; $G(n_i)$ is the target power spectral density function, which can be expressed as [44]:

$$G(n_i) = G(n_0)\left(\frac{n_i}{n_0}\right)^{-2} \tag{32}$$

where n_0 is reference spatial frequency; $G(n_0)$ is road roughness coefficient, determined by the road surface conditions. Class A is selected with $G(n_0) = 4 \times 10^{-6}$ m^3/cycles and $n_0 = 0.1$ cycles/m, in this case, since the Jizou Bridge is relatively new constructed. Considering the transverse correlation of road surface roughness [45], the road surface roughness at the windward wheel can be expressed as [1]:

$$R_W(x) = \sum_i^N \left[\gamma(n_i)\sqrt{2G(n_i)\Delta n}\cos(2\pi n_i x + \theta_i) + \sqrt{1-\gamma^2(n_i)}\sqrt{2G(n_i)\Delta n}\cos(2\pi n_i x + \varphi_i)\right] \tag{33}$$

where $\gamma(n_i)$ is the lateral coherence function; φ_i is the random phase angle uniformly distributed between 0 and 2π. A sample of the road surface roughness used in this case is presented in Figure 11.

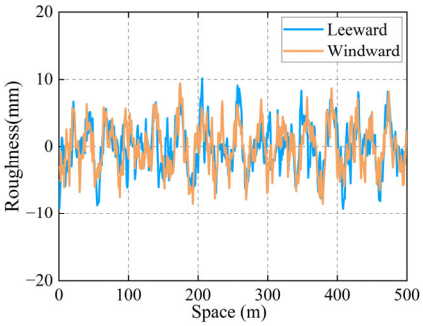


Figure 11. Simulated road surface roughness.

(4) Fluctuating wind

To obtain the gust wind-induced response, the Wavelet–Hilbert-based scheme was employed in the simulation of nonstationary fluctuating wind [33]. The fluctuating wind speed field with 95 discrete points distributed at 5 m intervals along the bridge axis was generated. Figure 12 shows the temporal and spatial distribution of the horizontal and vertical fluctuating wind at the bridge deck height. Meanwhile, the fluctuating wind on the vehicle is obtained with linear interpolation according to the initial location and the traveling velocity of vehicle, which was also schematically plotted in Figure 12.

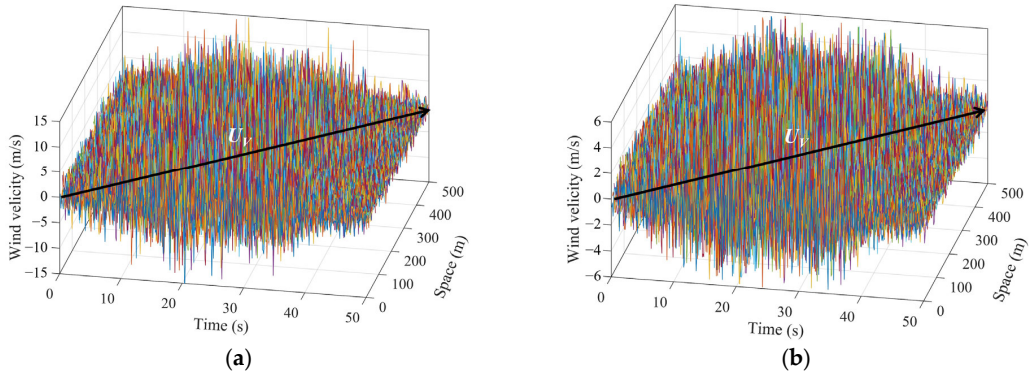


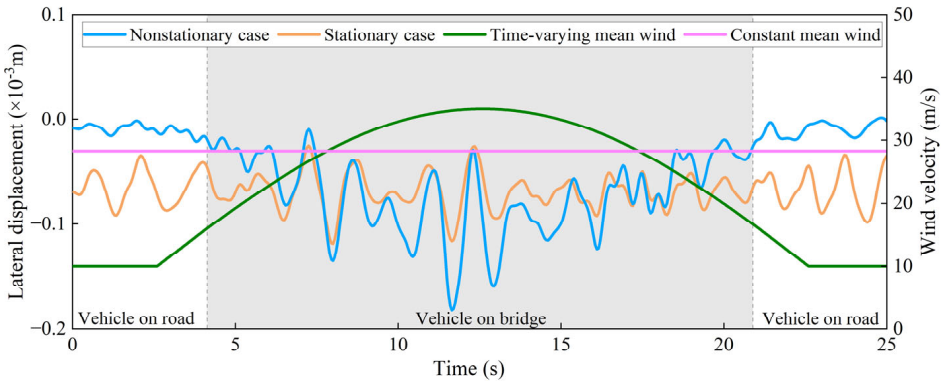
Figure 12. Simulated fluctuating wind (The colors represent different discrete points): (**a**) Horizontal direction. (**b**) Vertical direction.

4.2. Dynamic Response

The dynamic response of the nonstationary wind–vehicle–bridge coupling system was first investigated. The truck is assumed to travel with a constant speed of $U_v = 100$ km/h along the bridge span, and the transient wind velocity $U_{acc} = 25$ m/s and duration $T = 20$ s are selected. The maximum mean wind velocity occurs when the vehicle reaches the mid-span of the bridge, which may be the most detrimental to driving safety.

Figure 13 presents the time history of the displacements at the mid-span under nonstationary wind and vehicle loads. Meanwhile, the bridge response under the equivalent stationary wind is also plotted. The equivalent stationary wind is defined as the average of the time-varying mean wind over the duration (D_t is the time during which the vehicle travels on the bridge). Under stationary winds, the mid-span response oscillates around the static equilibrium position at a certain frequency due to the fluctuating wind. In the nonstationary case, the mid-span response increases with an increase in the mean wind velocity. Significant vibration of bridge occurs at the time when the mean wind speed reaches maximum, and the vehicle is located at the mid-span. The bridge response under nonstationary winds is significantly greater than that under stationary winds, primarily due to the stronger static wind effect induced by the nonstationary winds. This observation is similar to the results of wind tunnel tests regarding nonstationary wind-induced bridge response by Dong et al. [46]. Specifically, the maximum lateral, vertical, and torsional displacements under nonstationary winds are approximately 1.53, 1.48, and 1.35 times those in stationary case, respectively.

Figures 14 and 15 present the time histories of the wheel contact forces under stationary and nonstationary wind conditions, respectively. Under equivalent stationary winds, the wheel contact forces fluctuate around a constant mean force. At each time step, the sum of the vertical contact forces is approximately 29 kN, which is slightly lower than the vehicle weight (32.80 kN) due to the positive effects of the wind-induced lift force on the vehicle. The sum of the lateral contact forces is approximately 14 kN, corresponding to the steady-state lateral wind load on the vehicle. Furthermore, the vertical contact forces on the windward wheel are significantly smaller than those on the leeward wheel, as shown in Figure 14a, due to the crosswind effect. Notably, once the vertical contact force on the windward wheel becomes less than zero during the entire period, a rollover accident may occur under the current wind velocity (U_w = 28.27 m/s). Meanwhile, the lateral contact forces at the rear wheels are greater than those at the front wheels, as shown in Figure 14b, suggesting a higher potential risk of sideslip for the rear wheels.



(**a**)

Figure 13. *Cont.*

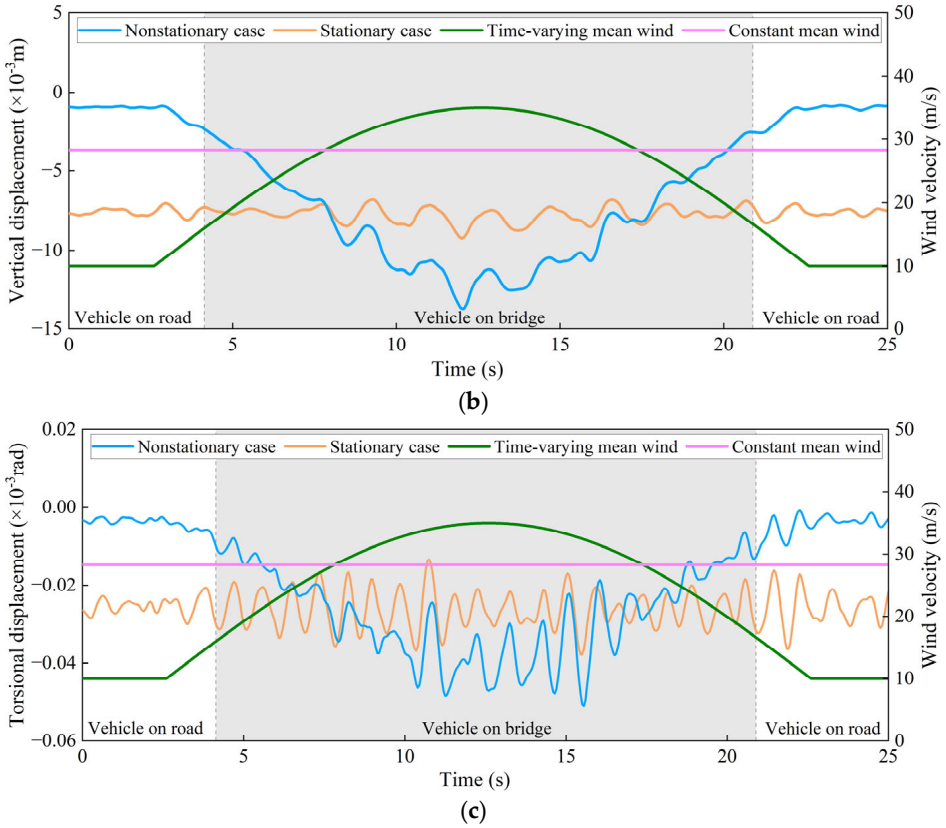


Figure 13. Displacements at mid-span of bridge: (**a**) Lateral direction. (**b**) Vertical direction. (**c**) Torsional direction.

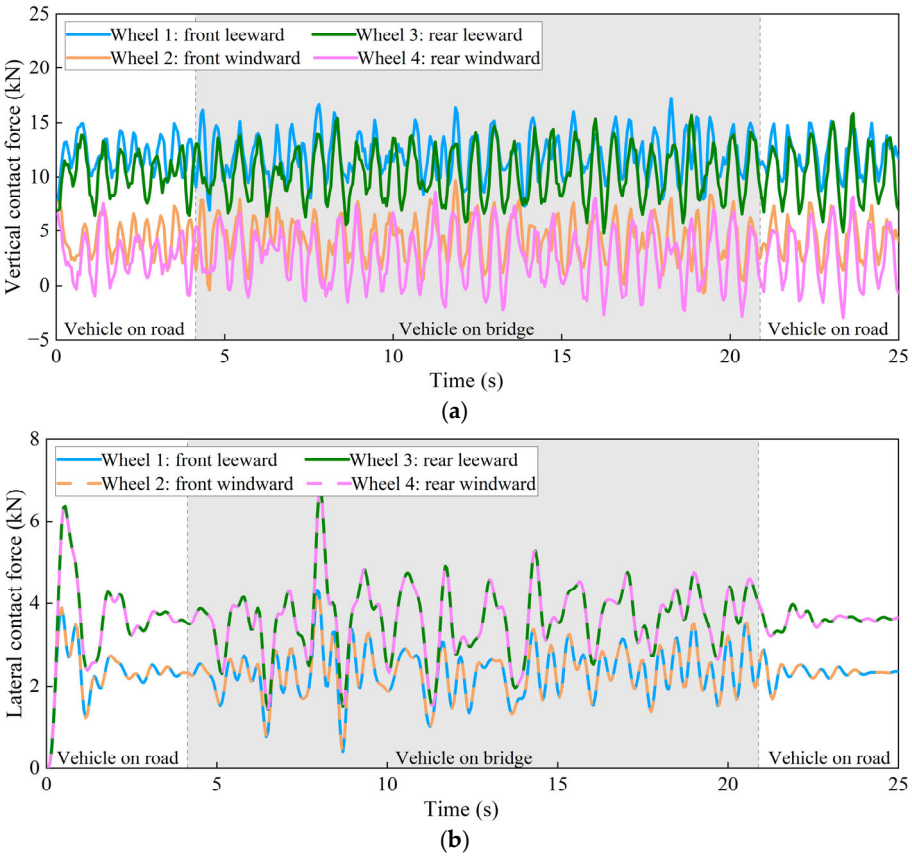


Figure 14. Wheel contact force under stationary wind. (**a**) Vertical direction. (**b**) Lateral direction.

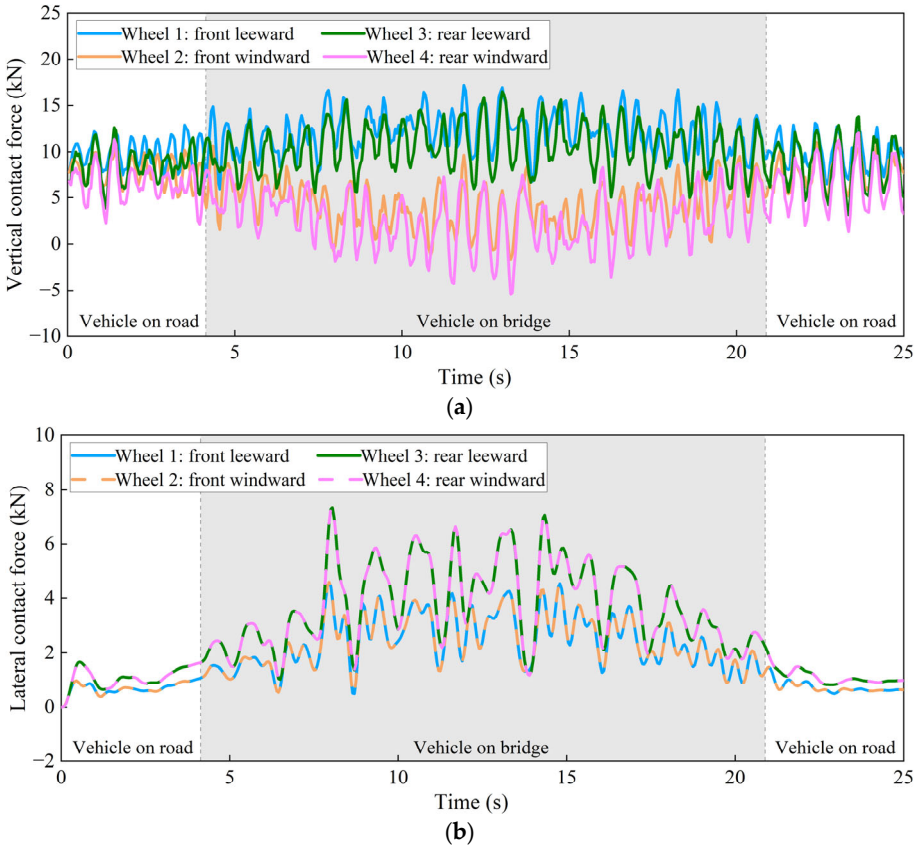


Figure 15. Wheel contact force under nonstationary wind. (**a**) Vertical direction. (**b**) Lateral direction.

Under nonstationary winds, the wheel contact forces also exhibit fluctuations, but with a noteworthy trend. This behavior could be primarily attributed to the variation in mean wind velocity. The reduction in vertical contact force in the windward wheel is larger than the increase in the leeward wheel, due to the wind-induced lift force on the vehicle. Compared to the equivalent stationary case, the transference of the vertical contact force from the windward to the leeward wheel is more significant under nonstationary wind. Also, the lateral contact forces under nonstationary wind are also greater than those in stationary case. These phenomena suggest that both rollover and sideslip accidents are more likely to occur under nonstationary winds.

Figure 16 shows the time histories of the rollover risk coefficient η_r and sideslip risk coefficient η_s for the truck on the bridge deck, which were calculated from the wheel contact forces according to Equations (28) and (29), respectively. Under nonstationary winds, higher risk coefficients are observed within the 8~16 s, which corresponds to the period of higher wind velocity. Under equivalent stationary winds, the risk coefficients remain relatively uniform throughout the vehicle traveling the bridge. According to the risk coefficients, both rollover and sideslip accidents are possible under stationary and nonstationary winds. But vehicle accidents, whether rollover or sideslip accidents, are more likely to occur under nonstationary winds compared to an equivalent stationary case. On the other hand, rollover accidents are more likely to occur for the vehicle on dry road surfaces, but the probability of rollover and sideslip accidents becomes comparable on wet road surfaces. Further discussion regarding driving safety will be presented in the following section.

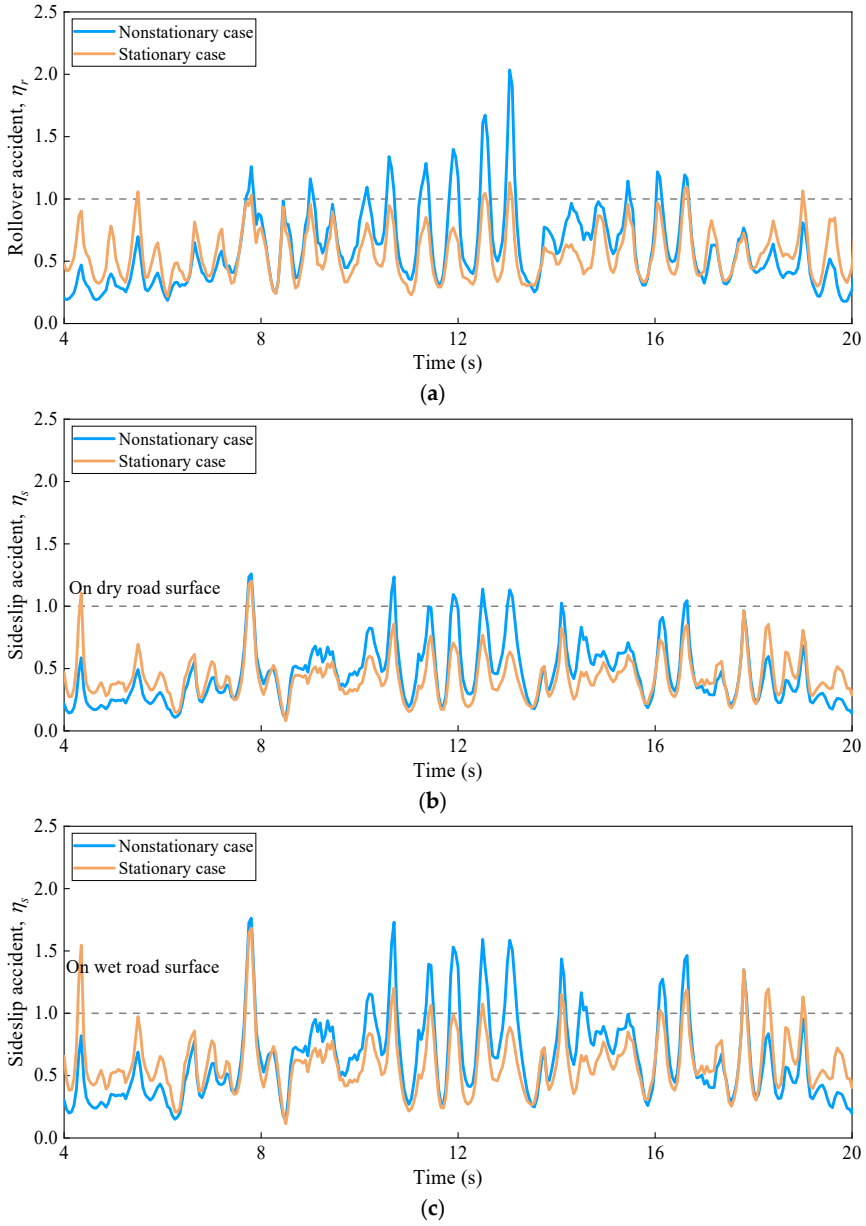


Figure 16. Accident risk coefficients (The dashed line represents the accident threshold): (**a**) Rollover. (**b**) Sideslip on dry road surface. (**c**) Sideslip on wet road surface.

Meanwhile, Figure 17 presents the distribution of the accident risk coefficients. Clearly, the accident risk coefficients obey a lognormal distribution, as checked by Kolmogorov–Smirnov (K-S) test.

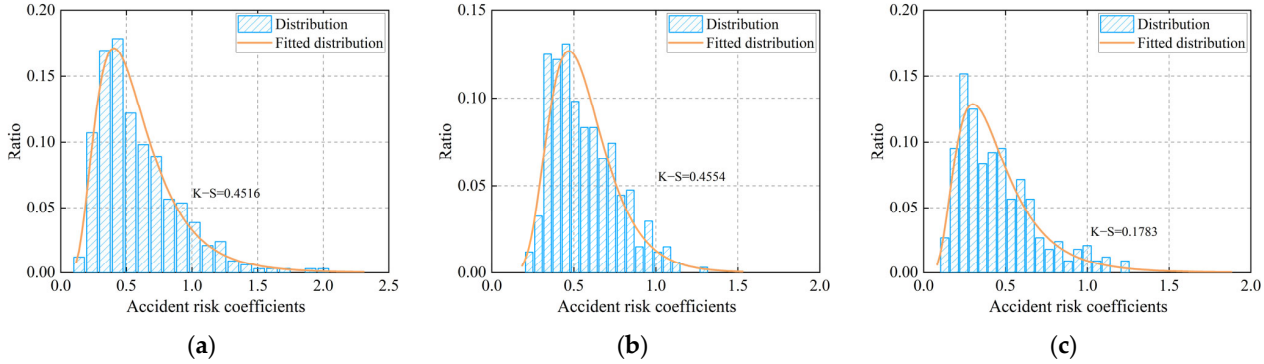


Figure 17. *Cont.*

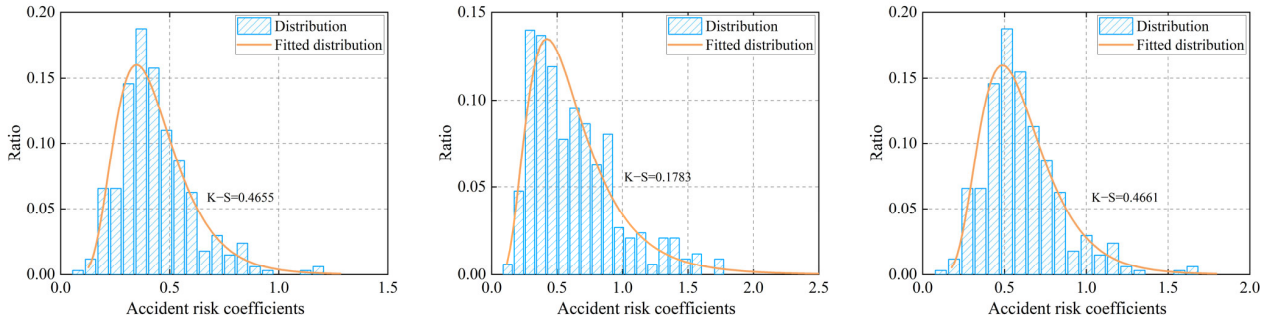


Figure 17. Distribution of accident risk coefficients: (**a**) Rollover risk coefficients in nonstationary case. (**b**) Rollover risk coefficients in stationary case. (**c**) Sideslip risk coefficients on dry surface in nonstationary case. (**d**) Sideslip risk coefficients on dry surface in stationary case. (**e**) Sideslip risk coefficients on wet surface in nonstationary case. (**f**) Sideslip risk coefficients on wet surface in stationary case.

4.3. Driving Safety Analysis

The computational results of the wind–vehicle–bridge system are actually a finite number of realizations of the coupled vibration random process. Therefore, the probability-based methods should be incorporated in the driving safety evaluation. In other words, the statistical values of vehicle accident risk coefficients should not be less than a specified quantile at a proper probability level, considering that the accident risk coefficients obey a lognormal distribution. Hence, the statistical value of the accident risk coefficients based on the probability distribution can be expressed as

$$\eta_r^* = \exp(\overline{m}_r + 1.645 v_r) \tag{34}$$

$$\eta_s^* = \exp(\overline{m}_s + 1.645 v_s) \tag{35}$$

where $\overline{m}$ are the location parameters in the lognormal distribution, $\overline{m} = \ln(\overline{\eta}^2 / \sqrt{\sigma^2 + \overline{\eta}^2})$; v are the scale parameters, $v = \sqrt{\ln(1 + \sigma^2/\overline{\eta}^2)}$; $\overline{\eta}$ and σ are the mean values and standard deviations of the rollover and sideslip risk coefficients; and the subscripts r and s represent rollover and sideslip accidents, respectively.

(1) Effect of maximum wind velocity

The statistical values of rollover and sideslip accident risk coefficients (η_r^* and η_s^*) for the vehicle traveling at $U_v = 100$ km/h under a transient wind duration of $T = 20$ s are plotted in Figure 18. With an increase in transient wind velocity, both the rollover and sideslip risk coefficients increase. The accident risk coefficients at a maximum wind velocity of 45 m/s are approximately 3.01 times those at a maximum wind velocity of 25 m/s. The accident risk coefficients under nonstationary winds are significantly higher than those under equivalent stationary winds, but the influence of nonstationary wind effects on the accident risk coefficients is insensitive to the transient wind velocity U_{acc}. The rollover risk coefficients for sedan and truck under nonstationary winds are approximately 1.87 and 1.25 times those under stationary winds. The sideslip risk coefficients for sedan and truck under nonstationary winds are approximately 1.20 and 1.38 times those under stationary winds. On the other hand, trucks on dry road surfaces are more prone to rollover accidents, while the probabilities of rollover and sideslip accidents become nearly comparable on wet road surfaces. Sedans are more likely to sideslip accidents and are almost impossible for rollovers.

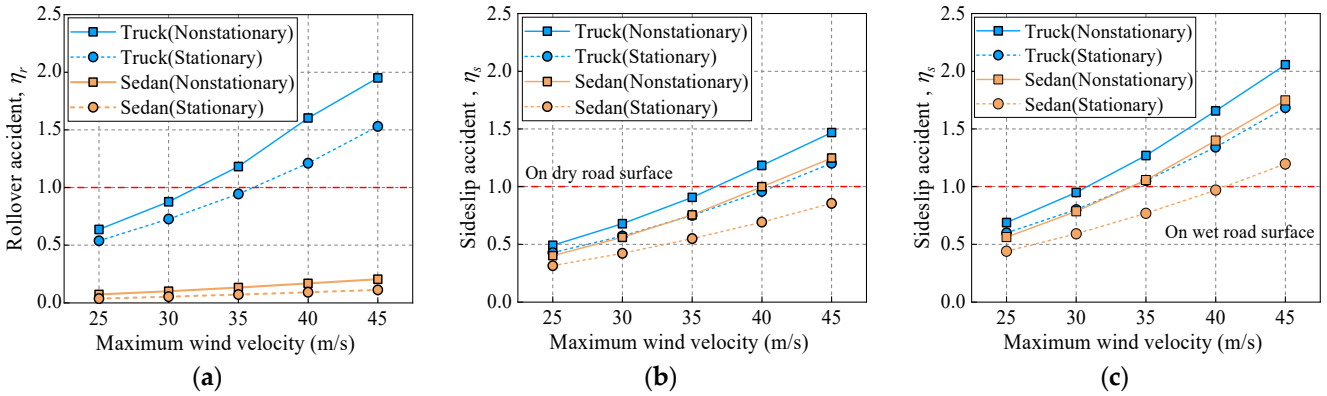


Figure 18. Accident risk coefficients with various maximum wind velocity (The red line represents the accident threshold): (**a**) Rollover. (**b**) Sideslip on dry road surface. (**c**) Sideslip on wet road surface.

(2) Effect of transient duration

The statistical values of rollover and sideslip accident risk coefficients (η_r^* and η_s^*) for the vehicle traveling at $U_v = 100$ km/h under a transient wind velocity of $U_{acc} = 25$ m/s are plotted in Figure 19. Under nonstationary winds, both rollover and sideslip accident risk coefficients are higher than those under equivalent stationary winds. The rollover and sideslip risk coefficients become higher with transient wind duration increasing, because the extended exposure to high wind velocity in the nonstationary case would also result in an increase in the equivalent constant mean wind velocity. The accident risk coefficient of sedan and truck increases by approximately 36.13% and 35.66%, respectively, with the increase in transient duration. However, the difference between nonstationary and stationary cases gradually diminishes with the transient duration increasing, because the time-varying mean wind would progressively approach a constant mean wind as transient duration increases. When the transient duration approaches infinity, the time-varying mean wind would effectively converge to a constant mean wind. On dry road surfaces, sideslip accidents are nearly impossible ($\eta_s^* < 1$), but the probabilities of rollover and sideslip accidents of trucks become almost comparable on wet road surfaces. Sedans on wet road surfaces may be likely to sideslip accidents with longer transient duration, but they are almost impossible for rollovers.

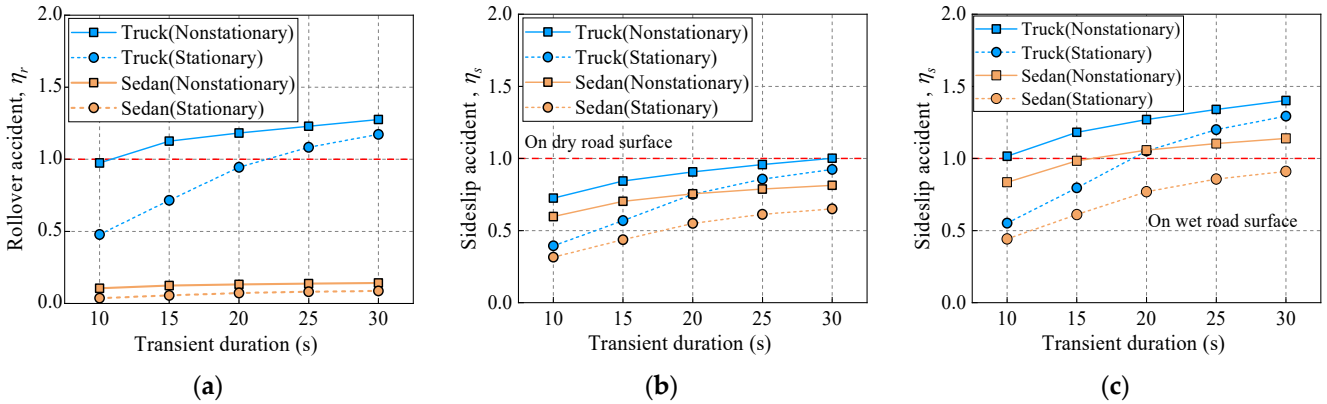


Figure 19. Accident risk coefficients with various transient duration (The red line represents the accident threshold): (**a**) Rollover. (**b**) Sideslip on dry road surface. (**c**) Sideslip on wet road surface.

(3) Effect of vehicle velocity

The statistical values of rollover and sideslip accident risk coefficients (η_r^* and η_s^*) for the vehicle under a transient wind velocity of $U_{acc} = 25$ m/s and duration of $T = 20$ s are

plotted in Figure 20. The increase in vehicle velocity would result in a higher resultant wind velocity U_R and wind loads on the vehicle, as well as the accident risk coefficients. The accident risk coefficient of sedan and truck increases by approximately 63.12% and 94.72%, respectively, with the increase in vehicle velocity. The vehicle accident risk coefficients under nonstationary winds are significantly higher than those under equivalent stationary winds. Interestingly, the risk coefficients of trucks remain almost unchanged in nonstationary case when the vehicle velocity increased from 100 km/h to 120 km/h. Also, the risk coefficients of sedans actually decreased slightly when the vehicle velocity increased from 120 km/h to 140 km/h. The reason behind the phenomenon is the nonlinear variation in vehicle aerodynamic coefficients with yaw angle. As shown in Figure 21, the maximum side force coefficient of sedans with $U_v = 140$ km/h is less than that with $U_v = 120$ km/h, as well as the side force coefficient of trucks with $U_v = 120$ km/h less than that with $U_v = 100$ km/h, which would result in smaller side force on vehicle and lower probability of sideslip risk.

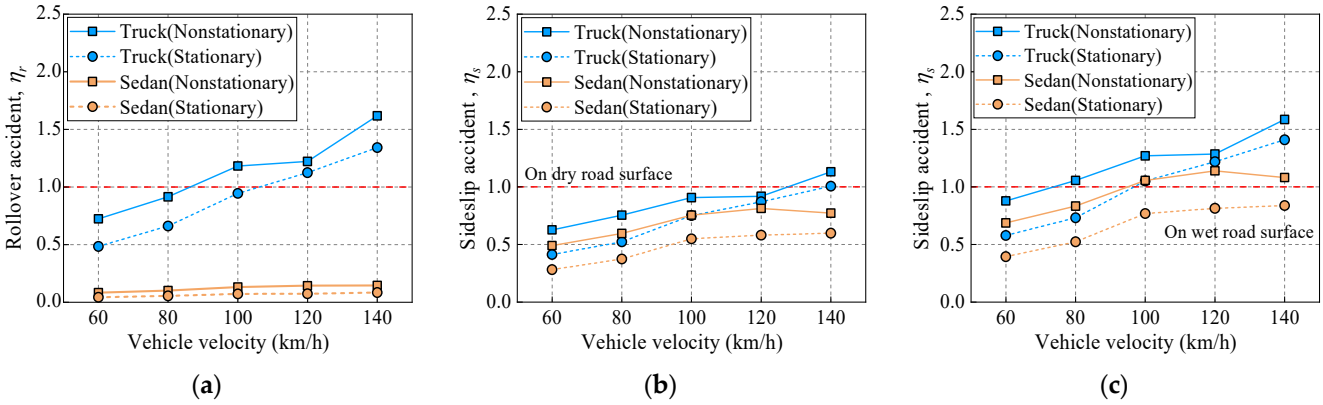


Figure 20. Accident risk coefficients with various vehicle velocity (The red line represents the accident threshold): (**a**) Rollover. (**b**) Sideslip on dry road surface. (**c**) Sideslip on wet road surface.

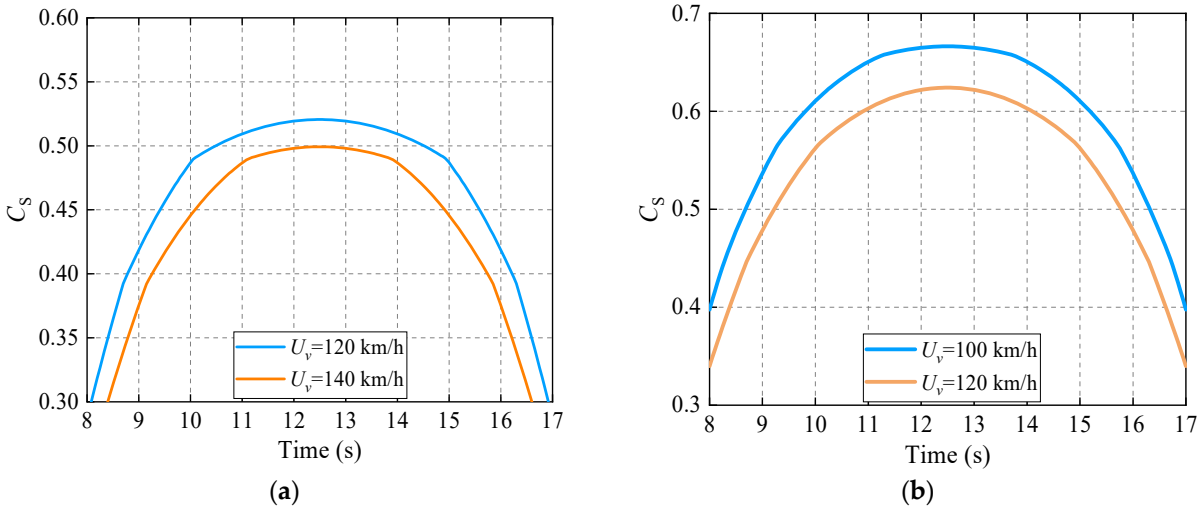


Figure 21. Time history of side force coefficients: (**a**) Sedan. (**b**) Truck.

5. Conclusions

In this study, the time-domain analysis framework for the wind–vehicle–bridge coupling system under nonstationary winds was established, in which the modeling of nonstationary wind fields and the aerodynamic loads were introduced. A cable-stayed bridge

was selected as a case to investigate the driving safety and performance of the coupling system in nonstationary wind events. The conclusions can be drawn as follows:

(1) The maximum bridge responses under nonstationary winds are larger than those resulting from equivalent stationary wind due to the higher static wind-induced effects in the nonstationary case.
(2) A higher unloading rate in the vertical contact forces of the windward wheels and larger lateral contact forces of the wheels were observed in the nonstationary case, which would result in a higher risk for the rollover and sideslip accidents.
(3) The statistical values of the vehicle accident risk coefficients increase as the transient wind, transient duration, and vehicle velocity increase, but the nonstationary effects on the accident risk coefficients would be significantly reduced with an increase in transient duration.
(4) The rollover accidents are more likely to occur when trucks travel on a dry road surface, but the probabilities of rollover and sideslip accidents are approximately the same when trucks travel on a wet road surface. Sedans are more likely to sideslip accidents and are almost impossible for rollovers.

Author Contributions: Conceptualization, Q.L. and G.Z.; methodology, Q.L.; software, G.Z.; validation, Y.F.; formal analysis, G.Z.; investigation, G.W.; resources, Q.L.; data curation, G.W.; writing—original draft preparation, Q.L.; writing—review and editing, Y.F.; visualization, G.W.; supervision, Q.L.; project administration, G.Z.; funding acquisition, Y.F. All authors have read and agreed to the published version of the manuscript.

Funding: This research was funded by Shandong Provincial Department of Transport Science and Technology Program, grant number 2024B58; Shandong Provincial Natural Science Foundation, grant number ZR2024QE042; and Shandong Provincial Natural Science Foundation, grant number ZR2025MS917.

Data Availability Statement: The original contributions presented in the study are included in the article, further inquiries can be directed to the corresponding author.

Conflicts of Interest: Author Qinghang Li and Guoxing Wang were employed by the company Shandong Pengcheng Road and Bridge Group Co., Ltd. Author Ganyu Zhou was employed by the company Innovation Research Institute of Shandong High-Speed Group Co., Ltd. The remaining authors declare that the research was conducted in the absence of any commercial or financial relationships that could be construed as a potential conflict of interest.

References

1. Yan, L.; Li, J.; He, X.; Li, Y. Ride comfort assessment of road vehicles on a long-span truss girder suspension bridge under crosswinds. *Eng. Struct.* **2025**, *322*, 119112. [CrossRef]
2. Hao, J.; Wu, T. Downburst-induced transient response of a long-span bridge: A CFD-CSD-based hybrid approach. *J. Wind Eng. Ind. Aerodyn.* **2018**, *179*, 273–286. [CrossRef]
3. Hoogewind, K.A.; Baldwin, M.E.; Trapp, R.J. The impact of climate change on hazardous convective weather in the United States: Insight from high-resolution dynamical downscaling. *J. Clim.* **2017**, *30*, 10081–10100. [CrossRef]
4. Baker, C. Measures to control vehicle movement at exposed sites during windy periods. *J. Wind Eng. Ind. Aerodyn.* **1987**, *25*, 151–161. [CrossRef]
5. Guo, W.; Xu, Y.L. Safety analysis of moving road vehicles on a long bridge under crosswind. *J. Eng. Mech.* **2006**, *132*, 438–446. [CrossRef]
6. Guo, J.; Ma, K. Risk analysis for hazardous chemical vehicle-bridge transportation system: A dynamic Bayesian network model incorporating vehicle dynamics. *Reliab. Eng. Syst. Saf.* **2024**, *242*, 109732. [CrossRef]
7. Liu, P. Analysis, Detection and Early Warning Control of Dynamic Rollover of Heavy Freight Vehicles. Ph.D. Thesis, Concordia University, Montreal, QC, Canada, 1999.
8. Wang, B.; Xu, Y.-L. Safety analysis of a road vehicle passing by a bridge tower under crosswinds. *J. Wind Eng. Ind. Aerodyn.* **2015**, *137*, 25–36. [CrossRef]

9. Cai, C.; Chen, S. Framework of vehicle–bridge–wind dynamic analysis. *J. Wind Eng. Ind. Aerodyn.* **2004**, *92*, 579–607. [CrossRef]
10. Han, Y.; Cai, C.; Zhang, J.; Chen, S.; He, X. Effects of aerodynamic parameters on the dynamic responses of road vehicles and bridges under cross winds. *J. Wind Eng. Ind. Aerodyn.* **2014**, *134*, 78–95. [CrossRef]
11. Camara, A.; Kavrakov, I.; Nguyen, K.; Morgenthal, G. Complete framework of wind-vehicle-bridge interaction with random road surfaces. *J. Sound Vib.* **2019**, *458*, 197–217. [CrossRef]
12. Zhu, S.; Li, Y.; Xu, X. Dynamic analysis of wind–vehicle–bridge systems: An advanced hybrid method. *Int. J. Struct. Stab. Dyn.* **2022**, *22*, 2250182. [CrossRef]
13. Zhang, J.; Zhu, C.; Ma, C. Driving safety analysis of wind–vehicle–bridge system considering aerodynamic interference. *J. Wind Eng. Ind. Aerodyn.* **2024**, *245*, 105649. [CrossRef]
14. Chen, N.; Wang, X.; Li, S.; Xiang, H. Safety analysis of road vehicles overtake on cables-Stayed bridge under crosswinds. *Adv. Struct. Eng.* **2023**, *26*, 870–887. [CrossRef]
15. Camara, A. Vehicle–bridge interaction and driving accident risks under skew winds. *J. Wind Eng. Ind. Aerodyn.* **2021**, *214*, 104672. [CrossRef]
16. Shen, J.; Wang, Z.; Qin, J.; Xiang, H.; Li, Y. Dynamic response of road vehicle–bridge system under wake-induced vertical vibration of long-span parallel cable-stayed bridges. *Int. J. Struct. Stab. Dyn.* **2026**, 2750182. [CrossRef]
17. Zou, Y.; Xue, F.; Shi, K.; He, X.; Han, Y.; Liu, Q.; Li, L. Analysis of the effects of wind barrier on driving safety and comfort of vehicles on long-span bridges under crosswinds. *Structures* **2022**, *42*, 367–385. [CrossRef]
18. Fu, Y.; Wu, F.; Chai, C.; Cui, W.; Li, Y.; Zhao, L. Assessment of driving safety and comfort during vortex-induced vibrations in a long-span bridge considering wind-vehicle-bridge interactions. *J. Wind Eng. Ind. Aerodyn.* **2025**, *257*, 106007. [CrossRef]
19. Fujii, T.; Maeda, T.; Ishida, H.; Imai, T.; Tanemoto, K.; Suzuki, M. Wind-induced accidents of train/vehicles and their measures in Japan. *Q. Rep. RTRI* **1999**, *40*, 50–55. [CrossRef]
20. McCullough, M.; Kwon, D.K.; Kareem, A.; Wang, L. Efficacy of averaging interval for nonstationary winds. *J. Eng. Mech.* **2014**, *140*, 1–19. [CrossRef]
21. Tao, T.; Wang, H.; Wu, T. Comparative study of the wind characteristics of a strong wind event based on stationary and nonstationary models. *J. Struct. Eng.* **2017**, *143*, 04016230. [CrossRef]
22. Wang, H.; Wu, T. Hilbert-wavelet-based nonstationary wind field simulation: A multiscale spatial correlation scheme. *J. Eng. Mech.* **2018**, *144*, 04018063. [CrossRef]
23. Lombardo, F.T.; Smith, D.A.; Schroeder, J.L.; Mehta, K.C. Thunderstorm characteristics of importance to wind engineering. *J. Wind Eng. Ind. Aerodyn.* **2014**, *125*, 121–132. [CrossRef]
24. Huang, G.; Peng, L.; Kareem, A.; Song, C. Data-driven simulation of multivariate nonstationary winds: A hybrid multivariate empirical mode decomposition and spectral representation method. *J. Wind Eng. Ind. Aerodyn.* **2020**, *197*, 104073. [CrossRef]
25. Feng, Y.; Hao, J.; Han, W.; Su, Q.; Wu, T. An optimized numerical tornado simulator and its application to transient wind-induced response of a long-span bridge. *J. Wind Eng. Ind. Aerodyn.* **2022**, *227*, 105072. [CrossRef]
26. He, X.-h.; Shi, K.; Wu, T. An efficient analysis framework for high-speed train-bridge coupled vibration under non-stationary winds. *Struct. Infrastruct. Eng.* **2020**, *16*, 1326–1346. [CrossRef]
27. Hu, J.; Lu, G.; Zhou, W.; Wu, H.; Zhang, S.; Miao, C. Analysis of Dynamic Response and Driving Safety of Ultra-High Pier Long-Span Rigid-Frame Bridge Under Nonstationary Wind. *Int. J. Struct. Stab. Dyn.* **2025**, 2650406. [CrossRef]
28. Xu, Y.-L.; Guo, W. Dynamic analysis of coupled road vehicle and cable-stayed bridge systems under turbulent wind. *Eng. Struct.* **2003**, *25*, 473–486. [CrossRef]
29. Bao, Y.; Li, Y.; Ding, J. A Case Study of Dynamic Response Analysis and Safety Assessment for a Suspended Monorail System. *Int. J. Environ. Res. Public Health* **2016**, *13*, 1121. [CrossRef] [PubMed]
30. Kwon, D.-K.; Kareem, A. Gust-front factor: New framework for wind load effects on structures. *J. Struct. Eng.* **2009**, *135*, 717–732. [CrossRef]
31. Feng, Y.; Su, Q.; Hao, J.; Han, W.; Wang, H. A comparative study on the transient wind-induced response of long-span bridges subject to downbursts and typhoons. *Eng. Struct.* **2023**, *280*, 115649. [CrossRef]
32. Wang, L.; McCullough, M.; Kareem, A. A data-driven approach for simulation of full-scale downburst wind speeds. *J. Wind Eng. Ind. Aerodyn.* **2013**, *123*, 171–190. [CrossRef]
33. Wang, H.; Wu, T. Time-varying multiscale spatial correlation: Simulation and application to wind loading of structures. *J. Struct. Eng.* **2020**, *146*, 04020138. [CrossRef]
34. Chen, X.; Matsumoto, M.; Kareem, A. Time domain flutter and buffeting response analysis of bridges. *J. Eng. Mech.* **2000**, *126*, 7–16. [CrossRef]
35. Wu, T.; Kareem, A. Revisiting convolution scheme in bridge aerodynamics: Comparison of step and impulse response functions. *J. Eng. Mech.* **2014**, *140*, 04014008. [CrossRef]
36. Hao, J.; Wu, T. Nonsynoptic wind-induced transient effects on linear bridge aerodynamics. *J. Eng. Mech.* **2017**, *143*, 04017092. [CrossRef]

37. Baker, C. The simulation of unsteady aerodynamic cross wind forces on trains. *J. Wind Eng. Ind. Aerodyn.* **2010**, *98*, 88–99. [CrossRef]
38. Bao, Y.; Zhai, W.; Cai, C.; Zhu, S.; Li, Y. Dynamic interaction analysis of suspended monorail vehicle and bridge subject to crosswinds. *Mech. Syst. Signal Process.* **2021**, *156*, 107707. [CrossRef]
39. Han, W.; Liu, H.; Wu, J.; Yuan, Y.; Chen, A. Dynamic analysis of long-span cable-stayed bridges under wind and traffic using aerodynamic coefficients considering aerodynamic interference. *Wind Struct.* **2017**, *24*, 405–430. [CrossRef]
40. Li, Y.; Qiang, S.; Liao, H.; Xu, Y.L. Dynamics of wind–rail vehicle–bridge systems. *J. Wind Eng. Ind. Aerodyn.* **2005**, *93*, 483–507. [CrossRef]
41. Han, W.; Ma, L.; Cai, C.S.; Chen, S.; Wu, J. Nonlinear dynamic performance of long-span cable-stayed bridge under traffic and wind. *Wind Struct.* **2015**, *20*, 249–274. [CrossRef]
42. Chen, N.; Li, Y.; Wang, B.; Su, Y.; Xiang, H. Effects of wind barrier on the safety of vehicles driven on bridges. *J. Wind Eng. Ind. Aerodyn.* **2015**, *143*, 113–127. [CrossRef]
43. Dodds, C.; Robson, J. The description of road surface roughness. *J. Sound Vib.* **1973**, *31*, 175–183. [CrossRef]
44. Wang, T.-L.; Huang, D. Cable-stayed bridge vibration due to road surface roughness. *J. Struct. Eng.* **1992**, *118*, 1354–1374. [CrossRef]
45. Bogsjö, K. Coherence of road roughness in left and right wheel-path. *Veh. Syst. Dyn.* **2008**, *46*, 599–609. [CrossRef]
46. Dong, X.; Zhao, L.; Cui, W.; Peng, Y.; Ge, Y. Aerodynamics and aeroelastic performance of a rigid-frame bridge with a bluff body girder subjected to short-rise-time gusts. *Eng. Struct.* **2022**, *263*, 114376. [CrossRef]

Disclaimer/Publisher's Note: The statements, opinions and data contained in all publications are solely those of the individual author(s) and contributor(s) and not of MDPI and/or the editor(s). MDPI and/or the editor(s) disclaim responsibility for any injury to people or property resulting from any ideas, methods, instructions or products referred to in the content.